ACSNANO

www.acsnano.org

ARTICLE

Coherent Lattice Wobbling and Out-of-Phase Intensity Oscillations of Friedel Pairs Observed by Ultrafast Electron Diffraction

Qingkai Qian, Xiaozhe Shen, Duan Luo, Lanxin Jia, Michael Kozina, Renkai Li, Ming-Fu Lin, Alexander H. Reid, Stephen Weathersby, Suji Park, Jie Yang, Yu Zhou, Kunyan Zhang, Xijie Wang, and Shengxi Huang*

Cite This: *ACS Nano* 2020, 14, 8449–8458

Read Online

ACCESS | Metrics & More | Article Recommendations | Supporting Information

ABSTRACT: The inspection of Friedel's law in ultrafast electron diffraction (UED) is important to gain a comprehensive understanding of material atomic structure and its dynamic response. Here, monoclinic gallium telluride (GaTe), as a low-symmetry, layered crystal in contrast to many other 2D materials, is investigated by mega-electronvolt UED. Strong out-of-phase oscillations of Bragg peak intensities are observed for Friedel pairs, which does not obey Friedel's law. As evidenced by the preserved mirror symmetry and supported by both kinematic and dynamic scattering simulations, the intensity oscillations are provoked by the lowest-order longitudinal acoustic breathing phonon. Our results provide a generalized understanding of Friedel's law in UED and demonstrate that by designed misalignment of surface normal and primitive lattice vectors, coherent lattice wobbling and effective shear strain can be generated in crystal films by laser pulse excitation, which is otherwise hard to achieve and can be further utilized to dynamically tune and switch material properties.

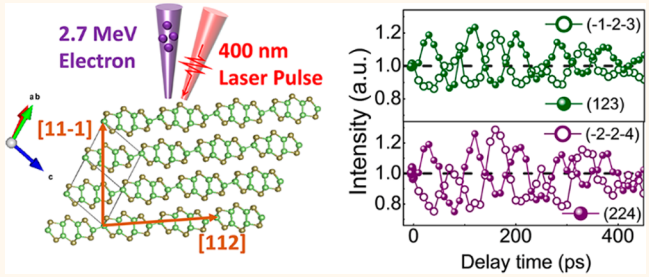

KEYWORDS: *GaTe, UED, Friedel pair, out-of-phase oscillation, shear strain*

Diffractions including X-ray, electron, and neutron scatterings, have become vital techniques in material and life sciences to reveal atomic structures and investigate material properties.[1−4] Friedel's law, first proposed by Georges Friedel for X-ray diffraction and also applicable to electron and neutron scatterings, has several forms of statements currently, which are not exactly equivalent. One form states that the diffraction intensities of a Friedel pair, *i.e.*, diffraction peaks of (hkl) and $(-h-k-l)$, are equal.[5,6] This statement is empirical and less rigorous, but can be easily compared with experimental results,[6] thus has been widely adopted.[7−10] This statement can be derived by Born approximation and the kinematic diffraction theory, which indicates that the scattering amplitudes are Fourier components of the real scattering potential and are thus complex conjugates to each other for a Friedel pair.[7] Another form of Friedel's law is "the diffraction phenomena of waves by a crystal are invariant under an inversion of the crystal".[6,11,12] This statement involves no ambiguity, but is not straightforward to directly compare with experimental results.[6] Therefore, the first statement in terms of diffraction intensities of Friedel pairs is adopted in our study.

Unequal intensities of Friedel pairs can be observed.[8−10,13,14] This phenomenon breaks Friedel's law, when Friedel's law is stated directly by equal intensities of Friedel pairs (the first statement),[8,9] or the equal intensities of Friedel pairs can be deduced according to the crystal symmetry in the second statement.[6,13,14] Currently, most reports about such unequal Friedel pair intensities, or breaking of Friedel's law, are conducted in static diffractions, caused by either the curvature of the Ewald sphere[8−10] or the dynamic scattering effects.[6,13,14] After a pump excitation (*e.g.*, ultrafast laser pulse), the time-resolved diffraction intensities of a Friedel pair can respond with opposite trends due to lattice dynamics, meaning that time-resolved unequal diffraction intensities of Friedel pairs or time-resolved violation of Friedel's law can be observed. Since the time-resolved diffractions can provide an additional degree

Received: March 28, 2020
Accepted: June 15, 2020
Published: June 15, 2020

https://dx.doi.org/10.1021/acsnano.0c02643
ACS Nano 2020, 14, 8449–8458

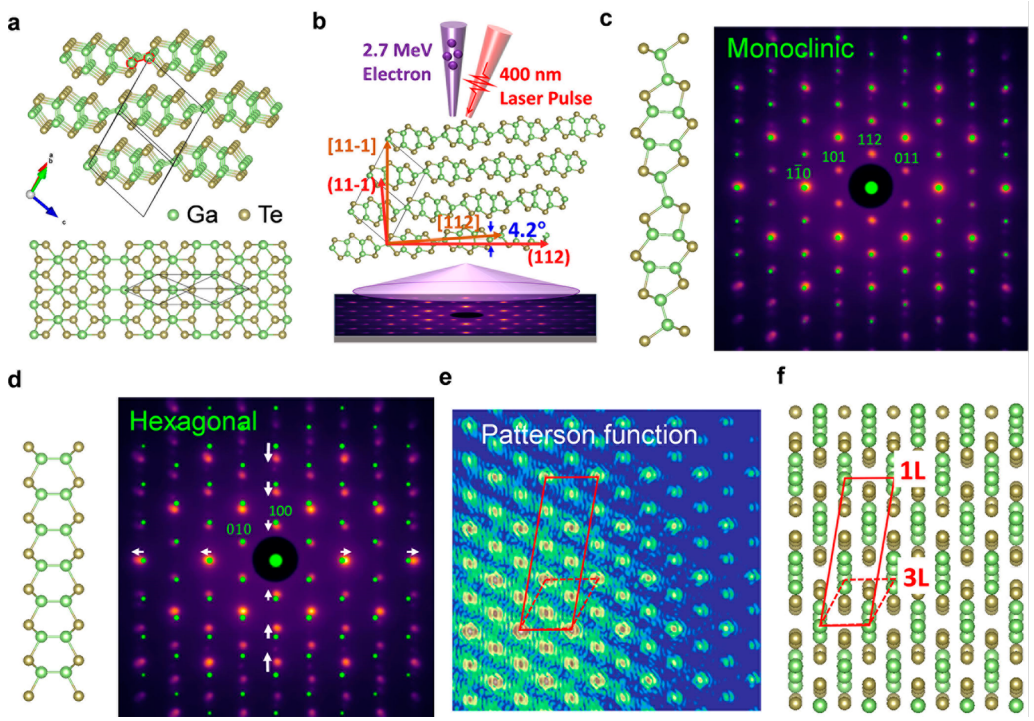

Figure 1. Hexagonal-like diffraction pattern of monoclinic GaTe. (a) Crystal structure of bulk monoclinic GaTe. Lower panel: Top view of monolayer GaTe. (b) Schematic illustration of MeV UED of GaTe. Incident electron is along the [11−1] axis. (c) Left: GaTe layer in monoclinic phase. Right: Electron diffraction pattern at 250 K and the simulated diffraction peaks (green dots) of monoclinic GaTe. (d) Left: GaTe layer in hexagonal phase. Right: Simulated diffraction peaks of hexagonal GaTe (green dots), compared with which the experimental results are compressed in one direction, due to the formation of in-plane Ga−Ga bonds in monoclinic GaTe. (e) Patterson function (*i.e.*, charge density correlation) of the electron diffraction pattern and (f) the projected atoms on the plane perpendicular to the incident electron beam.

of freedom in the time domain to investigate the material properties at nonequilibrium state,[1−4] the scrupulous inspection of Friedel's law in dynamic responses can promote the correct understanding and explanations of material properties in the pump−probe experiments.

Mega-electronvolt ultrafast electron diffraction (MeV UED), as a powerful pump−probe technique with high spatial and time resolutions,[15,16] has been widely used to study lattice dynamics.[2−4,17,18] The transient diffraction patterns measured by UED can unveil rich physics including phase transition,[18] the Debye−Waller effect,[4] or coherent phonons.[2,3,17] In these UED reports, the changes of diffraction intensities are mostly the same for each Friedel pair; namely, they obey Friedel's law. The underlying reason can be traced to the crystal symmetry and incident beam alignment of these studies. Taking the oscillations caused by the lowest-order breathing acoustic phonon mode in graphite as an example,[2] the breathing phonon mode is longitudinal, because it is excited by the thermal expansion of crystal lattices, while the transverse acoustic ones are usually hard to achieve.[19,20] When the electron beam is incident along the [001] direction, the diffraction pattern explicitly obeys Friedel's law, because the acoustic breathing phonon of graphite has a displacement vector aligned with the incident electron beam. Only by tilting the sample to a low-symmetry axis, such as the [212] direction in single-crystal TaSeTe (when the Friedel pair that breathes in opposite directions is cut by the Ewald sphere),[17] can out-of-phase intensity oscillations be experimentally observed, because of the breathing phonon and Ewald sphere curvature.[8−10,17] Distinctive from the previously studied 2D materials, monoclinic gallium telluride (GaTe) is a low-symmetry crystal,[21,22] which belongs to the $C2/m$ space group and has only four symmetry operations (*i.e.*, E, C_2, σ_h, and i). It can be expected that distinct lattice dynamics and diffraction features can be found in monoclinic GaTe. Besides, the diverse applications,[23,24] thickness-induced phase changes,[25] and surface reconstruction[26] of GaTe also made it an interesting material worth further investigation.

In this work, we use MeV UED to study the lattice dynamics of layered monoclinic GaTe, which shows coherent lattice wobbling and demonstrates the time-resolved asymmetry of Friedel pair intensities. Upon a femtosecond laser pulse excitation, strong oscillations of Bragg peak intensities are observed, and the oscillations are out-of-phase for each Friedel pair. The lowest-order longitudinal acoustic (LA) breathing phonon mode is responsible for the out-of-phase oscillations. Different from other high-symmetry 2D materials such as MoS_2 and graphite, the wave vector of the LA breathing mode of GaTe is misaligned with the Bravais lattice, which naturally causes a coherent wobbling of crystal lattice. Also different from the most-studied 2D materials, the diffraction pattern of GaTe is sensitive to surface flatness due to its nonorthogonal reciprocal lattices. Our results demonstrate a feasible way to engineer the coherent breathing phonon and effective shear strain in thin crystal films, which can be further used as a technique to dynamically modify and switch material properties. The out-of-phase oscillations of Friedel pair intensities also provide a more complete understanding of Friedel's law in UED.

https://dx.doi.org/10.1021/acsnano.0c02643
ACS Nano 2020, 14, 8449−8458

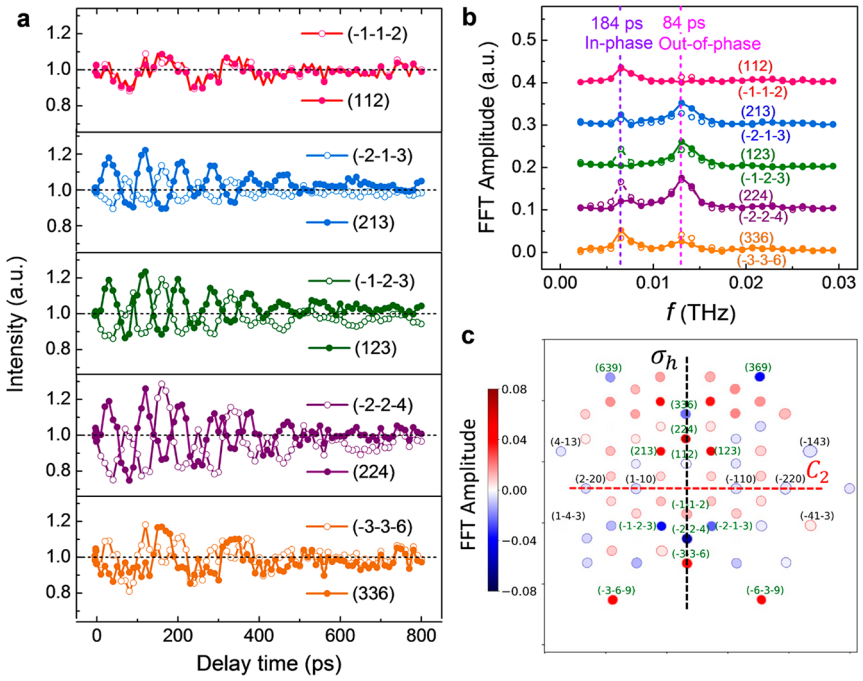

Figure 2. Out-of-phase intensity oscillations of Friedel pairs and the preserved symmetries. (a) Time evolution of Bragg peak intensities after laser pulse excitation at 250 K and (b) the corresponding fast Fourier transformation (FFT) amplitude. Strong out-of-phase oscillations with a period of 84 ps are observed for Friedel pairs. (c) FFT amplitudes and phases of Bragg peak intensities with a period of 84 ps. The Bragg peak with an initial increase of diffraction intensity after laser excitation is designated with a positive amplitude, while the out-of-phase one is designated with a negative amplitude. The dashed lines indicate the mirror-symmetry plane σ_h and 2-fold rotation axis C_2 of monoclinic GaTe.

RESULTS AND DISCUSSION

Large-area single-crystal GaTe films (99.999%, Alfa Aesar) are mechanically exfoliated and transferred on a copper grid. The detailed preparation process is described in the Methods section. Different from other widely studied 2D materials, bulk GaTe is in monoclinic phase and has lower symmetry.[21,22] Its crystal structure is shown in Figure 1a. It belongs to the *C*2/*m* space group, which has a 2-fold rotation axis C_2 ([1−10] direction) and a mirror plane σ_h symmetry.[22] The primitive unit cell consists of 6 Ga and 6 Te atoms. Bulk monoclinic GaTe has a direct bandgap of 1.6 eV.[27] A thickness-induced structural transformation between monoclinic and hexagonal phases has been reported.[25] Compared to its hexagonal phase, monoclinic GaTe features an in-plane Ga−Ga bond (highlighted by red in Figure 1a). The GaTe film is suspended on a copper grid (see Supporting Information Figure S1). The electron and laser beam sizes are about 70 and 500 μm, respectively, with the electron beam completely overlapped by the laser beam. The thicknesses of GaTe film in different areas are measured by scanning electron microscope (SEM) and verified by atomic force microscope (AFM). The GaTe film in the incident electron beam area has a thickness of 134 nm. MeV UED is used to investigate the structure dynamics of monoclinic GaTe. The incident electrons are generated by photoexciting a copper cathode using a 266 nm ultrafast laser pulse and then rapidly accelerated to a kinematic energy of 2.7 MeV. A 400 nm laser pulse is used as pump to excite the GaTe film. The relative time delay between the laser pump and electron probe is adjusted by a linear translation stage. A time resolution of 150 fs can be achieved by the whole system. The detailed MeV UED setups and specifications are described in the Methods section. The relativistic electron beam is incident along the [11−1] axis, which is almost perpendicular to the layers, but is still 4.2° deviated from the layer surface normal, as schematically drawn in Figure 1b.

Hexagonal-like Diffraction Pattern of Monoclinic GaTe. The electron diffraction pattern at 250 K is shown in Figure 1c, which has a hexagonal-like pattern. The green dots are the simulated diffraction pattern of monoclinic GaTe, with electrons incident along the [11−1] direction, which shows good agreement with the experimental results. A detailed comparison reveals that this hexagonal-like pattern is not exactly hexagonal. The hexagons are compressed along the (112) direction, as clearly evidenced in Figure 1d, which shows the simulated diffraction pattern of hexagonal GaTe. The reason that a hexagonal-like diffraction pattern is observed for monoclinic GaTe can be understood by the projection of atomic structures on the diffraction plane (plane perpendicular to the incident electron beam direction). Figure 1e plots the Patterson function of the experimental diffraction pattern, which also shows a hexagonal-like pattern. The Patterson function is the Fourier transformation of the diffraction pattern (see Methods section for details), which can be interpreted as the autocorrelation function of the projected charge density.[28] Figure 1f shows the projection of GaTe atoms in the [11−1] plane, which shares the same unit cell with the Patterson function in Figure 1e. The projected atoms of single-layer GaTe have a long parallelogram unit cell. However, for the projection of three GaTe layers, the repetition unit cell reduces to one-third of the previous one, which is very close to the unit cell of a honeycomb lattice and thus is responsible for the hexagonal-like diffraction pattern. Because of the in-plane Ga−Ga bonds in monoclinic GaTe, the honeycomb lattice is stretched along the (112) direction; as a result, the hexagonal-like Bragg peaks are compressed in the same direction.

https://dx.doi.org/10.1021/acsnano.0c02643
ACS Nano 2020, 14, 8449−8458

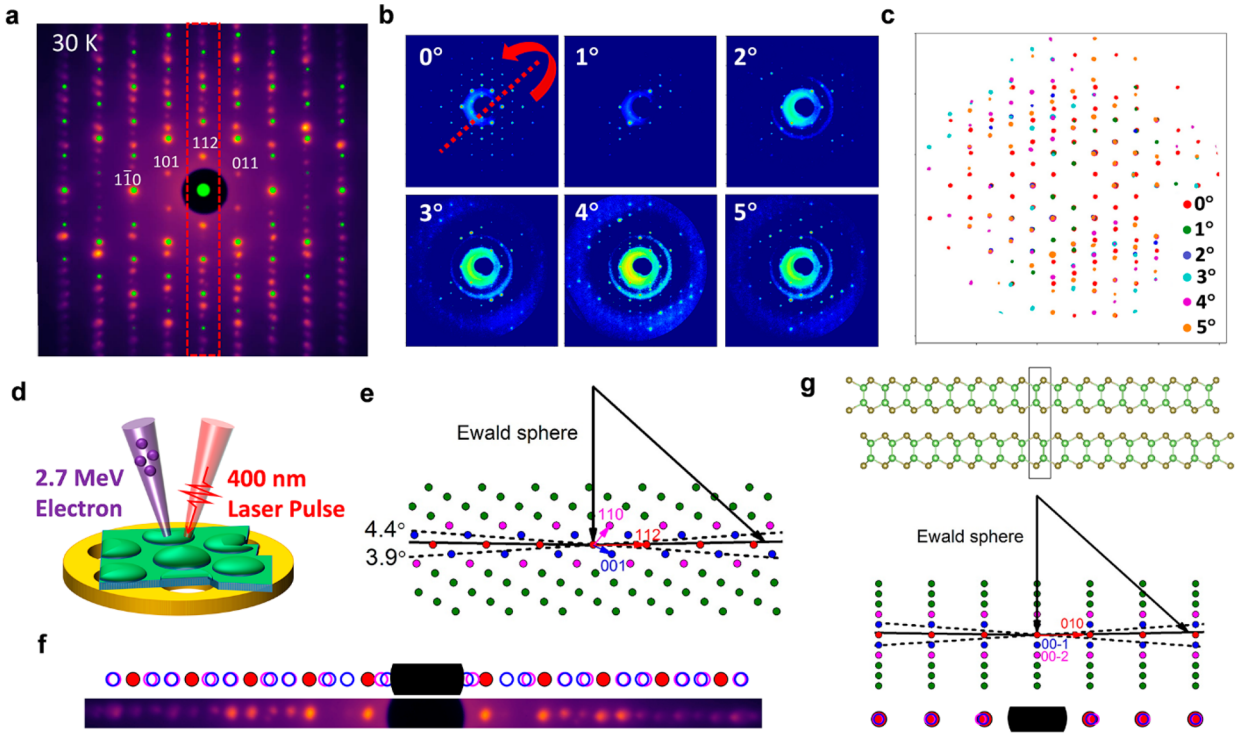

Figure 3. Sensitive diffraction pattern of monoclinic GaTe due to change of sample flatness at 30 K. (a) Electron diffraction pattern of suspended GaTe on a copper grid at 30 K. Besides peaks predicated by a monoclinic single crystal (green dots), new peaks have emerged. (b) Diffraction pattern of tilted GaTe on a Si_3N_4 grid at 30 K. (c) Overlapped Bragg peaks of diffraction patterns in (b). (d) Schematic illustration of bulged GaTe suspended on a copper grid. (e) Cut of out-of-plane reciprocal lattices of monoclinic GaTe by an Ewald sphere and (f) the resulting diffraction peaks along the (112) direction. The experimental result in (a) is also shown as a comparison. (g) Ewald sphere cut of a nonflat high-symmetry crystal (hexagonal GaTe) and the resulting diffraction peaks. Because of the vertically aligned reciprocal lattices, no discernible new Bragg peaks will be observed.

Out-of-Phase Intensity Oscillations of Friedel Pairs. A femtosecond laser pulse at a wavelength of 400 nm is used to excite the GaTe film (Figure 1b). The fluence of each laser pulse is 1.5 mJ/cm^2, with the laser polarized along the (112) direction. The dynamic responses of the diffraction pattern are recorded by scanning the time delay between the electron beam and laser pulse. Figure 2a plots the time evolutions of selected Bragg peak intensities, which are normalized by the static diffraction intensities before the laser pulse. The results for each Friedel pair (*i.e.*, (*hkl*) and (−*h*−*k*−*l*) Bragg peaks) are drawn together in one subplot. The Bragg peak intensity shows clear oscillation after laser excitation, especially for Friedel pairs including (213), (123), and (224) peaks. This strong oscillation is more clearly shown by the fast Fourier transformation (FFT) in Figure 2b, which indicates an oscillation period of 84 ps. The oscillations for each Friedel pair are out-of-phase; that is, the intensity of the Bragg peak (−*h*−*k*−*l*) oscillates with a 180° phase difference with that of the (*hkl*) peak. The Friedel pairs of (112) and (336) peaks oscillate weakly out-of-phase with a period of 84 ps, but oscillate relatively stronger in-phase with a period of 184 ps. The in-phase and out-of-phase oscillations can also be clearly distinguished by the FFT phases (see Supporting Information Figure S2). According to the adopted Friedel's law stated in the introduction, the diffraction intensities for Friedel pairs should be equal. Unequal intensities of the Friedel pair (or called violation of Friedel's law in some work) have been reported before in static electron diffraction and were explained by the Ewald sphere curvature[8−10] or a dynamic scattering theory.[13,14] Here, our out-of-phase oscillations of Friedel pairs show a time-resolved violation of Friedel's law.

The intensity oscillation amplitudes and phases are calculated for every Bragg peak and plotted in Figure 2c. Red-colored Bragg peaks indicate that the intensity oscillations have a 0° phase; that is, the diffraction intensity increases shortly after the laser excitation, just like the (224) peak in Figure 2a, while the blue ones indicate that the intensity oscillations are 180° out-of-phase. The magnitude of the FFT amplitudes (with 84 ps period) are represented by the absolution values of the color scales in the color bar. The oscillation amplitudes and phases of the Bragg peak intensities clearly show some symmetries, as indicated by the red and black dashed lines in Figure 2c. The mirror symmetry plane σ_h (black dashed line) is perpendicular to the paper. The oscillation amplitudes and phase are symmetric about this plane, indicating the lattice oscillations caused by the laser excitation have preserved this mirror symmetry. Because of this mirror symmetry and the out-of-phase oscillations of Friedel pairs, the oscillation phases are antisymmetric about the 2-fold rotation axis C_2. For Bragg peaks close to the C_2 axis, such as Bragg peaks (−110), (−220), and (−143) that are labeled in black, their intensity oscillations are very weak (see Supporting Information Figure S2).

Diffraction Patterns and Intensity Evolutions at 30 K. Figure 3a shows the diffraction pattern of the GaTe film at 30 K. The green dots are the simulated diffraction peaks of monoclinic GaTe, which match with the diffraction pattern measured at 250 K (Figure 1c). At 30 K, new Bragg peaks have emerged compared with 250 K. The disappearance and

https://dx.doi.org/10.1021/acsnano.0c02643
ACS Nano 2020, 14, 8449−8458

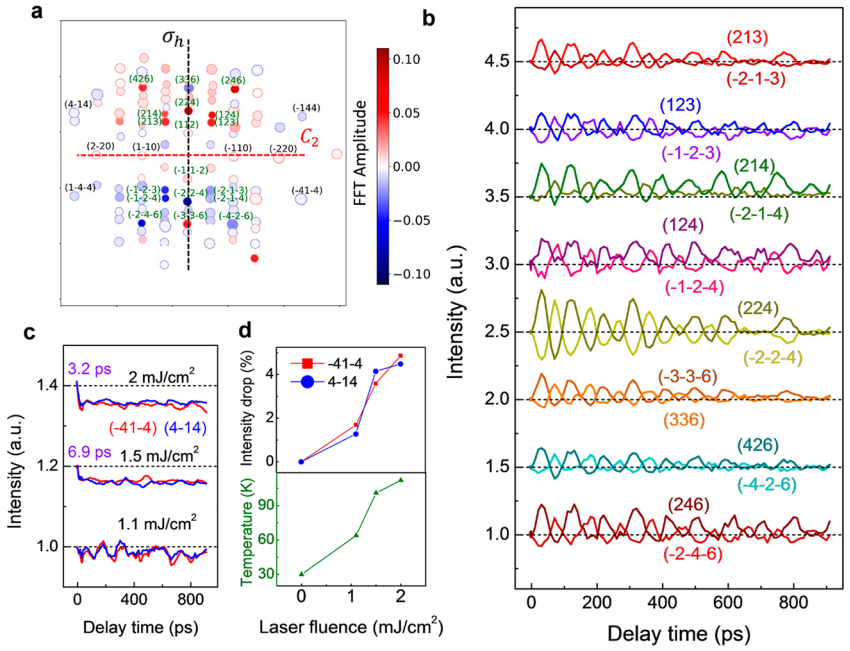

Figure 4. Out-of-phase intensity oscillations and Debye−Waller effect at 30 K. (a) FFT amplitudes and phases of Bragg peak intensities measured at 30 K. (b) Time evolution of Bragg peak intensities for selected Friedel pairs. The intensities are normalized and shifted vertically for a clear view. All Friedel pairs including the newly emerged ones show strong out-of-phase oscillations. (c) Diffraction intensity evolutions of Friedel pairs (−41−4) and (4−14) with increasing laser pulse fluence. (d) Corresponding intensity drop caused by the Debye−Waller effect and the calculated temperature.

emergence of the new Bragg peaks are reversible upon heating and cooling. The newly emerged peaks are closely aligned with the original ones (green dots) along the (112) direction, which are located almost at the trisection points of the original Bragg peaks. The gradual change of the diffraction pattern during the cooling process is shown in Supporting Information Figure S3. Similar diffraction patterns are observed for two other samples suspended on the copper grid (see Supporting Information Figure S4). However, no such phenomenon is observed for the GaTe film on the Si_3N_4 grid, the diffraction pattern of which always remains hexagonal-like. Clearly, the substrates have an influence over the diffraction patterns. One possible reason is that different substrates induce different sample flatness. Figure 3b records the diffraction patterns of a GaTe film on a Si_3N_4 grid during intentionally tilting the sample from 0° to 5°. The red dashed line shows the tilt axis. The halo in the diffraction pattern is caused by the scattering of the Si_3N_4 substrate. Bragg peaks far from the center vanish quickly after a 1° tilt, but new peaks emerge after a larger tilt, indicating the out-of-plane Bragg peaks are now cut by the Ewald sphere. All the Bragg peaks in Figure 3b are extracted and overlapped in Figure 3c for easier comparison. The overlapped Bragg peaks reproduce the diffraction pattern in Figure 3a, with the newly emerging Bragg peaks lying at the trisection points of the original Bragg peaks at 0° tilt.

Suspended GaTe film on a copper grid can be nonflat in the 70 μm × 70 μm diffraction region, especially after the sample is cooled. The copper grid and GaTe film have different thermal expansion coefficients: 17 × 10^{-6} K^{-1} for copper and 7.9 × 10^{-6} K^{-1} for GaTe.[29,30] During the cooling process, the thermal contraction difference can cause the bulging of the suspended GaTe film, as schematically drawn in Figure 3d. Recalling that the electron beam has a size of about 70 μm full width at half-maximum (fwhm), the GaTe film with different surface orientations is measured at the same time. Figure 3e shows the reciprocal lattice of monoclinic GaTe. When the sample is nonflat, for example, 5° deviated from the ideal incidence, not only the in-plane Bragg peaks (red) but also the out-of-plane ones (blue and pink) can be cut by the Ewald sphere and become observable. Figure 3f presents the Bragg spots along the (112) direction that can be cut by the Ewald sphere, which shows good agreement with the experimental results. Quantitative comparisons of the Bragg peak distances can be found in Supporting Information Figure S5. A suspended thin film on a TEM grid has been widely used for electron diffraction study.[31,32] However, for the previously studied 2D materials with high symmetry, a mild sample nonflatness will not change the diffraction pattern. Taking hexagonal GaTe in Figure 3g as an example, its reciprocal lattice vectors are vertically aligned. Even though the Ewald sphere cuts the out-of-plane reciprocal lattices, the projected Bragg peaks will still locate at almost the same positions. In contrast, monoclinic GaTe has reciprocal lattices that are not vertically aligned, making the influence of surface nonflatness more easily discernible.

Upon laser pulse excitation, the strong oscillations of Bragg peak intensities are also observed at 30 K. Figure 4a shows the oscillation amplitudes and phases. The intensity evolutions of several selected Friedel pairs are plotted in Figure 4b. Out-of-phase oscillations are observed for all these Friedel pairs, which is also evident in the FFT amplitude/phase map. Bragg peaks that have already been observed at 250 K maintain the same oscillations. The newly emerged Bragg peaks at 30 K, such as (214), (124), and their Friedel pairs, also show strong out-of-phase oscillations. Compared with the intensity oscillations at 250 K in Figure 2a, there are no significant in-phase oscillations of Bragg peak intensities at 30 K, making the out-of-phase intensity oscillations of the same (336) Friedel

https://dx.doi.org/10.1021/acsnano.0c02643
ACS Nano 2020, 14, 8449−8458

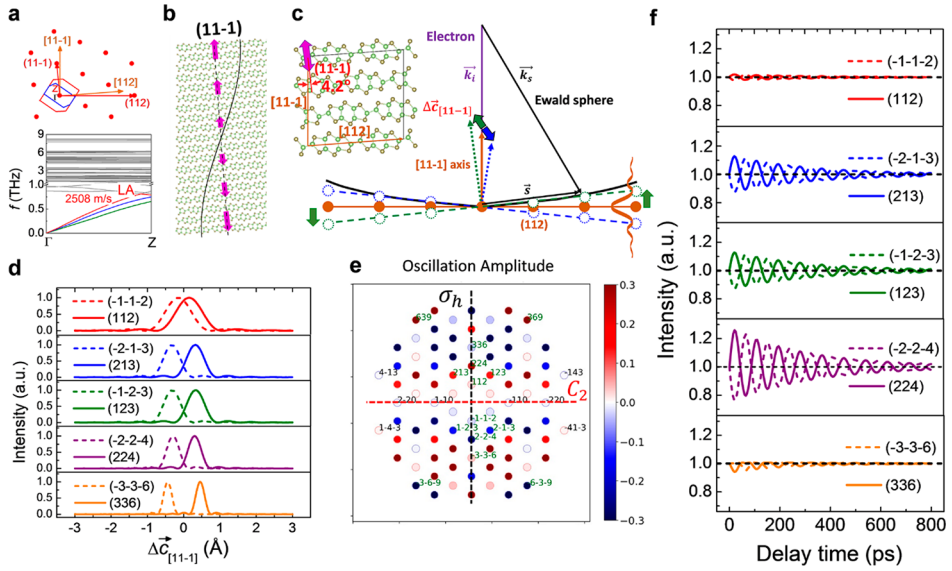

Figure 5. Coherent lattice wobbling and out-of-phase intensity oscillations caused by the misaligned LA breathing phonon. (a) Reciprocal lattices of monoclinic GaTe. The red and blue hexagons are the first Brillouin zones of the primitive unit cell ($a = b$) and the simple unit cell ($\beta = \gamma = 90°$) of monoclinic GaTe. Lower panel: Phonon dispersion along the (11−1) direction. (b) Schematics of the lowest-order longitudinal acoustic (LA) breathing mode. (c) Rotation of reciprocal lattices caused by the LA breathing mode. The blue and green arrows show the corresponding displacement of supercell axis [11−1] ($\Delta\vec{c}_{[11-1]}$) caused by the LA phonon. Inset: Created supercell to simplify the diffraction analysis; the purple arrow is the direction of vibration that causes $\Delta\vec{c}_{[11-1]}$. (d) Calculated diffraction intensities as a function of $\Delta\vec{c}_{[11-1]}$. (e) Calculated oscillation amplitudes and phases of Bragg peaks in one map. (f) Time evolution of selected Bragg peak intensities.

pairs more obvious here. The FFT amplitudes of Bragg peak intensities are plotted in Supporting Information Figure S6. The oscillation period increases slightly from 84 ps at 250 K to 92 ps at 30 K. Bragg peaks near the 2-fold rotation axis C_2 show consistent weak oscillations at 30 K (see Supporting Information Figure S6). The laser pulse polarization shows no significant influence over the Bragg peak intensities. At large laser pulse fluence, a strong Debye−Waller effect is observed for Bragg peaks with large momentum (see Supporting Information Figure S7). For Bragg peaks in Figure 2a and Figure 4b, because of their relatively small scattering momenta, there is no obvious Debye−Waller effect. Figure 4c plots the intensity evolutions of Bragg peaks (4−14) and (−41−4) with laser fluence. With the increase of laser pulse fluence from 1.1 mJ/cm^2 to 2 mJ/cm^2, the diffraction intensity drop caused by the Debye−Waller effect clearly becomes more evident, and the decay time also becomes shorter. The Debye−Waller effect is caused by the lattice thermal fluctuations, the amplitude of which can be calculated by the equation[4,33]

$$I = I_0 e^{-q^2\langle u_q^2\rangle} \quad (1)$$

in which I_0 is the diffraction intensity without lattice vibrations, q is the Bragg peak momentum, and u_q^2 is the mean square displacement of atoms along q and is calculated by the equation[34]

$$\langle u_q^2\rangle = \frac{3\hbar^2}{2mk_B\theta_D}\left[\frac{2T}{\theta_D}D_1\left(\frac{\theta_D}{T}\right) + \frac{1}{2}\right] \quad (2)$$

in which θ_D is the Debye temperature, k_B is the Boltzmann constant, T is sample temperature, m is the average atomic mass, and $D_1(x)$ is the first-order Debye function. Debye temperature can be estimated by $\theta_D = h\upsilon_s(3N/4\pi V)^{1/3}/k_B$,[35] in which υ_s is sound velocity and N/V is the atomic density. Taking υ_s = 3400 m/s,[36] the Debye temperature can be estimated to be θ_D = 326 K, which predicts a heat capacity of 47 J·mol^{-1}·K^{-1} at 300 K according to the Debye model and is consistent with the reported heat capacity of 49 J·mol^{-1}·K^{-1}.[37] From the intensity drop caused by laser pulse heating and the Debye−Waller effect in Figure 4c, the actual sample temperature T can be estimated from eq 2 and is plotted as a function of laser pulse fluence in Figure 4d.

Lattice Wobbling Caused by Misaligned LA Breathing Phonon. The out-of-phase oscillations of Bragg peak intensities for Friedel pairs are observed for two other samples as well (see Supporting Information Figure S8). The oscillation amplitudes and phases show sample dependence, and the oscillation frequency also varies. A thicker sample has longer oscillation period, and the oscillation frequency is much lower than that of the typical optical phonon. All this evidence suggests that the Bragg peak intensity oscillations are caused by acoustic phonons. Figure 5a shows the reciprocal lattice of monoclinic GaTe. The incident electron is along the [11−1] direction, while the layer surface normal vector is along (11−1). The first Brillouin zone of the primitive unit cell is drawn by the red hexagon in the upper plot, while the blue hexagon is the first Brillouin zone of the simple unit cell ($\beta = \gamma = 90°$). Phonon dispersion of GaTe obtained by first-principles calculations using the monoclinic simple unit cell is shown in the lower panel of Figure 5a. The frequencies of the observed oscillation fit well into the acoustic phonon frequency range. The lowest-order LA breathing phonon mode is most likely to be the source driving the observed oscillations, which is initiated by the thermal expansion of the heated thin film and has been observed for other 2D materials such as MoS_2 and graphite as well.[2,17,38,39] We note that an in-plane propagating or standing acoustic wave across the whole GaTe film could also have a reasonable oscillation frequency comparable to the out-of-phase Bragg peak intensity oscillations here. However, the suspended GaTe film size under the electron beam (70

https://dx.doi.org/10.1021/acsnano.0c02643
ACS Nano 2020, 14, 8449−8458

μm) is much larger than the film thickness (134 nm), while the acoustic wavelength is limited by the sound velocity and the oscillation period. As a result, compared with the lowest-order LA breathing mode, the in-plane propagating or standing wave across the film has many oscillation peaks and valleys, which will cancel each other due to the phase difference at different locations and cannot account for the coherent out-of-phase intensity oscillations of Friedel pairs observed in our experiment.

A schematic illustration of the lowest-order LA breathing mode in monoclinic GaTe is shown in Figure 5b. Both the wave vector and atomic displacement vector are perpendicular to the film surface. Based on the oscillation period T and film thickness D, the LA sound velocity can be calculated by $\nu = 2D/T$ to be 2910 m/s,[2,17,38,40] which is in good agreement with the theoretical calculation result in Figure 5a. The deviation with 3400 m/s in previous publications can be due to different sound velocities along different directions.[36] Different from other high-symmetry crystals, such as MoS_2 and graphite, the wave vector of the LA breathing phonon of monoclinic GaTe is naturally misaligned with the Bravais lattice vector by 4.2°. To simplify the analysis, a supercell is created with the original [−110], [112], and [11−1] vectors as the new primitive vectors, as shown in the inset of Figure 5c. The LA breathing phonon causes the tilting of the Bravais lattice because of its shear component due to the 4.2° misalignment. Because the reciprocal vector is always perpendicular to the Bravais lattice vector, this LA breathing phonon will cause the wobbling of reciprocal lattices, as schematically and exaggeratedly drawn in Figure 5c, which will periodically cut the Ewald sphere and cause the oscillation of diffraction intensities.

According to the Born approximation and the kinematic scattering theory, the diffraction intensity can be calculated by the equation[7]

$$I(\vec{s}) = |f_{\text{supercell}}(\vec{s})|^2 \left| \frac{\sin(N/3\cdot\vec{s}\cdot(\vec{c}_{[11-1]} + \Delta\vec{c}_{[11-1]})/2)}{\sin(\vec{s}\cdot(\vec{c}_{[11-1]} + \Delta\vec{c}_{[11-1]})/2)} \right|^2 \quad (3)$$

in which $f_{\text{supercell}}(\vec{s})$ is the scattering contribution of atoms in one supercell, N is the total GaTe layer number, $\vec{s}$ is the scattering vector, $\vec{c}_{[11-1]}$ is the supercell axis vector in Figure 5c, and $\Delta\vec{c}_{[11-1]}$ is the change of this axis caused by the LA breathing phonon. We note that we have ignored the sinusoidal waveform of the LA breathing phonon and approximated it by a linear lattice strain to get this analytic expression, which captures the most fundamental influence of the lowest-order LA phonon. Based on this equation, diffraction intensities for selected Bragg peaks are calculated in Figure 5d, as a function of the displacement of the supercell axis $\vec{c}_{[11-1]}$. The Friedel pairs show equal diffraction intensities at zero $\vec{c}_{[11-1]}$ displacement. The intensity curves for Friedel pairs with large momenta have narrower peak widths and a faster change of diffraction intensities, which can be understood by the tilting of the reciprocal lattice in Figure 5c. The Bragg spot shows strength oscillation due to the thickness-dependent fringes in reciprocal space. The Friedel pair with large momenta is further away from the Ewald sphere and takes larger lattice rotation to be cut, so it takes larger axis displacement to reach peak intensity in Figure 5d; it also moves faster with the tilting of the lattice, so it has a smaller peak width and faster intensity variation.

The LA breathing phonon causes the tilt of the [11−1] axis and thus the wobbling of both Bravais and reciprocal lattices. As can be seen in Figure 5d, the intensity curves are symmetric about zero $\vec{c}_{[11-1]}$ displacement for each Friedel pair. As the LA breathing phonon periodically tilts the [11−1] axis, the diffraction intensities of Friedel pairs will change in opposite trends and oscillate with a 180° different phase. A more exact solution of the diffraction intensity oscillations caused by the LA breathing phonon is provided in Figure 5e and f using kinematic scattering theory, which has included the exact sinusoidal waveform of the LA breathing mode and assumes the immediate expansion of GaTe layers upon laser pulse excitation. The oscillation amplitudes and phases for all Bragg peaks are calculated and plotted in one map in Figure 5e. The Bragg peaks with small scattering momenta show good agreement with the experimental results in Figure 2c, including those near the 2-fold rotation axis C_2 with weak intensity oscillations. Alternatively, dynamic scattering simulations using a two-beam model or the multislice frozen phonon method yield very similar diffraction patterns (see Supporting Information Figures S9 and S10).[7,41] Some discrepancies between experiment and theory are observed for peaks with large momentum, such as Bragg peaks (639) and (369). We note that for Bragg peaks with large momentum, the diffraction intensities are weak because the diffraction deviation is relatively large and the Ewald sphere only cuts the fringes. The GaTe film in the nonflat region may be cut right into the Bragg peak center and has a larger diffraction intensity, which will contribute more to the observed diffraction intensity and can be responsible for the deviations of theoretical calculations.

The calculation results for selected Bragg peaks are plotted in Figure 5f, which show good agreement with the experimental results in Figure 2a, in terms of both oscillation amplitudes and phases. A decay time of 312 ps for the LA phonon is used, which is extracted by fitting of the Bragg peak (224) intensity in Figure 2a. The LA breathing amplitude is found to be 0.46 Å at the film surface, which is consistent with our theoretically estimated breathing phonon amplitude and further validates our LA breathing phonon analysis above (see Supporting Information Figures S11−S14). This LA breathing phonon has an energy of 1.8×10^{-4} mJ/cm^2. By considering the refractive index of GaTe film at 400 nm,[27] the laser absorption rate can be calculated to be 62%, which indicates that about 1.9×10^{-4} of the absorbed laser energy is converted to this breathing mode.

CONCLUSIONS

In this work, we have used MeV UED to study the lattice dynamics of layered monoclinic GaTe and observed coherent lattice wobbling and the out-of-phase oscillations of Friedel pair intensities. Monoclinic GaTe shows a hexagonal-like diffraction pattern, with the hexagons compressed in one direction, due to the formation of in-plane Ga−Ga bonds. The nonorthogonal reciprocal lattice of monoclinic GaTe has made the diffraction pattern more sensitive to sample flatness, in contrast to other high-symmetry crystals. After pulsed laser excitation, strong coherent oscillations of Bragg peak intensities are observed at both low and high temperatures. The oscillations are out-of-phase for each Friedel pair, which is caused by the lowest-order LA breathing phonon mode, as evidenced by the symmetry analysis and supported by both kinematic and dynamic simulations. The monoclinic crystal structure of the GaTe film naturally makes the displacement

https://dx.doi.org/10.1021/acsnano.0c02643
ACS Nano 2020, 14, 8449−8458

vector of LA breathing phonon mode misaligned with the Bravais lattices, which causes the wobbling of both Bravais and reciprocal lattices and is responsible for the out-of-phase oscillations. Similar phenomena should be expected in other low-symmetry 2D materials such as monoclinic $MnPS_3$ and triclinic ReS_2.[42,43] While shear lattice strain is usually hard to achieve,[19,20] the misaligned LA phonon with respect to the Bravais lattice vector has created both longitudinal and shear strains in monoclinic GaTe layers after a simple laser pulse excitation. As widely reported, strain could provide a natural means to tune the material properties, especially for materials in which the crystalline symmetry is vital.[3,44] By misalignment of the primitive lattice and its surface normal vector, which can be practically realized, for example using focused ion beam milling, our results demonstrate a practical way to induce ultrafast and switchable shear strain in materials and may find applications in sensors and nanomechanical/optomechanical systems.[45]

METHODS

Sample Preparation. Bulk GaTe crystals were purchased from Alfa Aesar (gallium(II) telluride, 99.999%, metals basis). The GaTe crystal was exfoliated into thin flakes on adhesive tape (3M Scotch magic), which was then pasted on melted Crystalbond (SPI Supplies, Inc.) on a glass slide. After the Crystalbond was cooled to room temperature and solidified, the adhesive tape was peeled off. Thin GaTe films were left on the Crystalbond. Crystalbond was then dissolved in water. The GaTe flakes were then fished on a TEM grid or can be dropped on a copper or silicon nitride TEM grid using a pipet. The copper grid has holes of 150 μm size. The silicon nitride grid has no holes. The sample was left to dry naturally.

MeV Ultrafast Electron Diffraction. The MeV ultrafast electron diffraction was conducted in the Accelerator Structure Test Area facility at the SLAC National Laboratory.[16] The 400 nm (3.1 eV) laser, which was generated by frequency doubling of a 60 fs 800 nm Ti:sapphire laser at a repetition rate of 180 Hz, was focused to the sample with about a fwhm spot size of 474 μm × 579 μm. The electron beam was generated using the frequency-tripled laser by excitation of a copper photocathode and rapidly accelerated to 2.7 MeV (kinetic energy) in radiofrequency electric fields. The electron beam was normally incident on the sample with a fwhm spot size of 70 μm × 70 μm. The relative arrival time delay between laser pulse and electron beam was adjusted by a linear translation stage. The diffraction pattern was imaged by a phosphor screen (P43) and recorded by an electron-multiplying charge-coupled device camera (Andor iXon Ultra 888).

DFT Calculation. Phonon dispersions of single-layer GaTe were calculated by VASP and Phonopy codes. VASP was used to optimize the ground-state lattice structure and obtain the force constants. Supercells created from 4 × 1 × 2 monoclinic simple unit cells ($\beta = \gamma = 90°$) were used, which have 192 atoms. The plane-wave basis was set with a cutoff energy of 400 eV. K-points with 2 × 4 × 3 gamma-centered grids in reciprocal space were adopted. The PBE functional and PAW potentials were adopted, with the van der Waals interaction corrected by the DFT-D3. The lattice was optimized until all forces were smaller than 0.01 eV/Å. Force constants were calculated by the finite difference method. Based on the force constants, phonon dispersion can be calculated by Phonopy codes.

Patterson Function. Different from X-ray scattering, both the nucleus and electron charges will contribute to the electrostatic potential during electron diffraction. The Patterson function was calculated by the Fourier transformation of the diffraction intensity $I(\vec{k})$ multiplied by scattering momentum $\vec{k}$ to the power of 4, as required by the Mott–Bette formula for the conversion between Coulomb potential and charge,[7] more specifically, $p(r) = \int I(\vec{k})|\vec{k}|^4 e^{-i\vec{k}\cdot\vec{r}} d^3k$. This Patterson function can be interpreted as the autocorrelation function of the projected charge density on the diffraction plane.[28]

Kinematic and Dynamic Scattering Simulations. During kinematic scattering and the two-beam model calculation, the electron scattering form factors of Ga and Te atoms were calculated by the Mott–Bethe formula,[7] $f(\vec{k}, Z) \propto (Z - f_X(\vec{k}, Z))/|\vec{k}|^2$, in which $\vec{k}$ is the scattering momentum, Z is the atomic number, and $f_X(\vec{k}, Z)$ is the X-ray scattering form factor. Numerical values of X-ray scattering form factors were taken from the International Tables for Crystallography.[46] The multislice dynamic simulation was conducted using the MULTEM program. MULTEM uses the multislice method, which can realize more accurate and fast simulation of diffraction intensity by solving the high-energy Schrodinger equation. To realize the mutlislice simulation of this relatively thick sample here, the atomic structure was constructed by vertically cutting the GaTe film with a rectangular box (95.9 Å × 96.5 Å × 1341 Å), which preserves the crystal periodicity in the x–y (in-layer) direction. The whole atomic structure consists of 180 GaTe layers and 414 720 atoms. The incident electron wave was tilted by 4.2° to the [11−1] direction. The atomic potential developed by Lobato was used. Grids of 1024 × 1024 in the x–y direction were adopted, while the z direction was cut through atomic planes. Frozen phonon calculation was performed by using the Einstein model with 50 configurations and a three-dimensional RMS displacement of 0.085 Å. The effect of the LA phonon was simulated by creating atomic structures under different oscillation phases of the LA breathing mode, which always preserves the crystal periodicity in the x–y direction.

ASSOCIATED CONTENT

Supporting Information

The Supporting Information is available free of charge at https://pubs.acs.org/doi/10.1021/acsnano.0c02643.

FFT phase for selected Bragg peaks. Diffraction pattern of the GaTe film during the cooling process; extracted Bragg peaks of flat GaTe film on Si_3N_4 substrate; dynamic response for three different GaTe samples suspended on copper grids with different laser polarization and laser pulse fluence; two-beam model and multislice method to simulate the dynamic diffraction intensity (PDF)

AUTHOR INFORMATION

Corresponding Author

Shengxi Huang − *Department of Electrical Engineering, The Pennsylvania State University, University Park, Pennsylvania 16802, United States;* orcid.org/0000-0002-3618-9074; Email: sjh5899@psu.edu

Authors

Qingkai Qian − *Department of Electrical Engineering, The Pennsylvania State University, University Park, Pennsylvania 16802, United States;* orcid.org/0000-0001-7513-0676

Xiaozhe Shen − *SLAC National Accelerator Laboratory, Menlo Park, California 94025, United States*

Duan Luo − *SLAC National Accelerator Laboratory, Menlo Park, California 94025, United States*

Lanxin Jia − *Department of Electrical Engineering, The Pennsylvania State University, University Park, Pennsylvania 16802, United States*

Michael Kozina − *SLAC National Accelerator Laboratory, Menlo Park, California 94025, United States*

Renkai Li − *Department of Engineering Physics, Tsinghua University, Beijing 100084, China*

Ming-Fu Lin − *SLAC National Accelerator Laboratory, Menlo Park, California 94025, United States*

https://dx.doi.org/10.1021/acsnano.0c02643
ACS Nano 2020, 14, 8449−8458

Alexander H. Reid − *SLAC National Accelerator Laboratory, Menlo Park, California 94025, United States*
Stephen Weathersby − *SLAC National Accelerator Laboratory, Menlo Park, California 94025, United States*
Suji Park − *SLAC National Accelerator Laboratory, Menlo Park, California 94025, United States*
Jie Yang − *SLAC National Accelerator Laboratory, Menlo Park, California 94025, United States*
Yu Zhou − *Department of Electrical Engineering, The Pennsylvania State University, University Park, Pennsylvania 16802, United States*
Kunyan Zhang − *Department of Electrical Engineering, The Pennsylvania State University, University Park, Pennsylvania 16802, United States*
Xijie Wang − *SLAC National Accelerator Laboratory, Menlo Park, California 94025, United States*

Complete contact information is available at: https://pubs.acs.org/10.1021/acsnano.0c02643

Author Contributions

Q.Q., L.J., and K.Z. prepared the GaTe samples. Q.Q., X.S., D.L., M.K., R.L., M.L., A.H.R., S.W., S.P., J.Y., and S.H. carried out the MeV UED experiments. Q.Q. carried out the data analysis and diffraction simulations. Q.Q., X.S., D.L., J.Y., Y.Z., X.W., and S.H. discussed the results. The experiment was conceived and supervised by X.W. and S.H.

Notes

The authors declare no competing financial interest.

ACKNOWLEDGMENTS

The UED work was conducted at SLAC MeV- UED, which is supported in part by the DOE BES SUF Division Accelerator & Detector R&D program, the LCLS Facility, and SLAC under contract nos. DE-AC02-05-CH11231 and DE-AC02-76SF00515. S.H. acknowledges the support from the National Science Foundation under grant number ECCS-1943895.

REFERENCES

(1) Mannebach, E. M.; Nyby, C.; Ernst, F.; Zhou, Y.; Tolsma, J.; Li, Y.; Sher, M.; Tung, I.; Zhou, H.; Zhang, Q.; Seyler, K. L.; Clark, G.; Lin, Y.; Zhu, D.; Glownia, J. M.; Kozina, M. E.; Song, S.; Nelson, S.; Mehta, A.; Yu, Y.; et al. Dynamic Optical Tuning of Interlayer Interactions in the Transition Metal Dichalcogenides. *Nano Lett.* **2017**, *17*, 7761−7766.
(2) Chatelain, R. P.; Morrison, V. R.; Klarenaar, B. L.; Siwick, B. J. Coherent and Incoherent Electron-Phonon Coupling in Graphite Observed with Radio-Frequency Compressed Ultrafast Electron Diffraction. *Phys. Rev. Lett.* **2014**, *113*, 235502.
(3) Sie, E. J.; Nyby, C. M.; Pemmaraju, C. D.; Park, S. J.; Shen, X.; Yang, J.; Hoffmann, M. C.; Ofori-Okai, B. K.; Li, R.; Reid, A. H.; Weathersby, S.; Mannebach, E.; Finney, N.; Rhodes, D.; Chenet, D.; Antony, A.; Balicas, L.; Hone, J.; Devereaux, T. P.; Heinz, T. F.; et al. An Ultrafast Symmetry Switch in a Weyl Semimetal. *Nature* **2019**, *565*, 61−66.
(4) Mannebach, E. M.; Li, R.; Duerloo, K.; Nyby, C.; Zalden, P.; Vecchione, T.; Ernst, F.; Reid, A. H.; Chase, T.; Shen, X.; Weathersby, S.; Hast, C.; Hettel, R.; Coffee, R.; Hartmann, N.; Fry, A. R.; Yu, Y.; Cao, L.; Heinz, T. F.; Reed, E. J.; et al. Dynamic Structural Response and Deformations of Monolayer MoS_2 Visualized by Femtosecond Electron Diffraction. *Nano Lett.* **2015**, *15*, 6889−6895.
(5) Friedel, G. Sur Les Symétries Cristallines Que Peut Révéler La Diffraction Des Rayons X. *C.R. Acad. Sci. Paris* **1913**, *157*, 1533−1536.
(6) Miyake, S.; Uyeda, R. Friedel's Law in the Dynamical Theory of Diffraction. *Acta Crystallogr.* **1955**, *8*, 335−342.
(7) Cowley, J. M. *Diffraction Physics*, third revised ed.; North Holland: Amsterdam, 1995.
(8) Fei, Z.; Wang, B.; Ho, C.; Lin, F.; Yuan, J.; Zhang, Z.; Jin, C. Direct Identification of Monolayer Rhenium Diselenide by an Individual Diffraction Pattern. *Nano Res.* **2017**, *10*, 2535−2544.
(9) Hoppe, W. Principles of Electron Structure Research at Atomic Resolution Using Conventional Electron Microscopes for the Measurement of Amplitudes and Phases. *Acta Crystallogr.* **1970**, *A 26*, 414−426.
(10) Xiong, D.; Lu, L.; Wang, J.; Zhao, D.; Sun, Y. Non-Centro-Symmetric Electron Diffraction Pattern of Icosahedral Quasicrystal Induced by Combination of Linear Phason Strain and Curvature of Ewald Sphere. *Micron* **2013**, *52*−*53*, 45−48.
(11) Spence, J. C. H.; Zuo, J. M. *Electron Microdiffraction*; Plenum Press: New York, 1992.
(12) Foss, O.; Zachariasen, H. The Crystal Structure of Barium Pentathionate Dihydrate. *Acta Chem. Scand.* **1954**, *8*, 473.
(13) Susi, T.; Madsen, J.; Ludacka, U.; Mortensen, J. J.; Pennycook, T. J.; Lee, Z.; Kotakoski, J.; Kaiser, U.; Meyer, J. C. Efficient First Principles Simulation of Electron Scattering Factors for Transmission Electron Microscopy. *Ultramicroscopy* **2019**, *197*, 16−22.
(14) Wang, Z.; Ning, S.; Fujita, T.; Hirata, A.; Chen, M. Unveiling Three-Dimensional Stacking Sequences of 1T Phase MoS_2 Monolayers by Electron Diffraction. *ACS Nano* **2016**, *10*, 10308−10316.
(15) Park, H. S.; Baskin, J. S.; Barwick, B.; Kwon, O.; Zewail, A. H. 4D Ultrafast Electron Microscopy: Imaging of Atomic Motions, Acoustic Resonances, and Moiré Fringe Dynamics. *Ultramicroscopy* **2009**, *110*, 7−19.
(16) Shen, X.; Li, R. K.; Lundström, U.; Lane, T. J.; Reid, A. H.; Weathersby, S. P.; Wang, X. J. Femtosecond Mega-Electron-Volt Electron Microdiffraction. *Ultramicroscopy* **2018**, *184*, 172−176.
(17) Wei, L.; Sun, S.; Guo, C.; Li, Z.; Sun, K.; Liu, Y.; Lu, W.; Sun, Y.; Tian, H.; Yang, H.; Li, J. Dynamic Diffraction Effects and Coherent Breathing Oscillations in Ultrafast Electron Diffraction in Layered 1T-TaSeTe. *Struct. Dyn.* **2017**, *4*, 44012.
(18) Kogar, A.; Zong, A.; Dolgirev, P. E.; Shen, X.; Straquadine, J.; Bie, Y.; Wang, X.; Rohwer, T.; Tung, I.; Yang, Y.; Li, R.; Yang, J.; Weathersby, S.; Park, S.; Kozina, M. E.; Sie, E. J.; Wen, H.; Jarillo-Herrero, P.; Fisher, I. R.; Wang, X.; et al. Light-Induced Charge Density Wave in $LaTe_3$. *Nat. Phys.* **2020**, *16*, 159−163.
(19) Matsuda, O.; Wright, O. B.; Hurley, D. H.; Gusev, V. E.; Shimizu, K. Coherent Shear Phonon Generation and Detection with Ultrashort Optical Pulses. *Phys. Rev. Lett.* **2004**, *93*, 95501.
(20) Rossignol, C.; Rampnoux, J. M.; Perton, M.; Audoin, B.; Dilhaire, S. Generation and Detection of Shear Acoustic Waves in Metal Submicrometric Films with Ultrashort Laser Pulses. *Phys. Rev. Lett.* **2005**, *94*, 166106.
(21) Sanchez-Royo, J. F.; Segura, A.; Munoz, V. Anisotropy of the Refractive Index and Absorption Coefficient in the Layer Plane of Gallium Telluride Single Crystals. *Phys. Status Solidi A* **1995**, *151*, 257−265.
(22) Huang, S.; Tatsumi, Y.; Ling, X.; Guo, H.; Wang, Z.; Watson, G.; Puretzky, A. A.; Geohegan, D. B.; Kong, J.; Li, J.; Yang, T.; Saito, R.; Dresselhaus, M. S. In-Plane Optical Anisotropy of Layered Gallium Telluride. *ACS Nano* **2016**, *10*, 8964−8972.
(23) Liu, F.; Shimotani, H.; Shang, H.; Kanagasekaran, T.; Zólyomi, V.; Drummond, N.; Fal Ko, V. I.; Tanigaki, K. High-Sensitivity Photodetectors Based on Multilayer GaTe Flakes. *ACS Nano* **2014**, *8*, 752−760.
(24) Dong, J.; Gradwohl, K.; Xu, Y.; Wang, T.; Zhang, B.; Xiao, B.; Teichert, C.; Jie, W. Terahertz Emission from Layered GaTe Crystal Due to Surface Lattice Reorganization and In-Plane Noncubic Mobility Anisotropy. *Photonics Res.* **2019**, *7*, 518.
(25) Zhao, Q.; Wang, T.; Miao, Y.; Ma, F.; Xie, Y.; Ma, X.; Gu, Y.; Li, J.; He, J.; Chen, B.; Xi, S.; Xu, L.; Zhen, H.; Yin, Z.; Li, J.; Ren, J.; Jie, W. Thickness-Induced Structural Phase Transformation of

Layered Gallium Telluride. *Phys. Chem. Chem. Phys.* **2016**, *18*, 18719−18726.
(26) Fonseca, J. J.; Tongay, S.; Topsakal, M.; Chew, A. R.; Lin, A. J.; Ko, C.; Luce, A. V.; Salleo, A.; Wu, J.; Dubon, O. D. Bandgap Restructuring of the Layered Semiconductor Gallium Telluride in Air. *Adv. Mater.* **2016**, *28*, 6465−6470.
(27) Leveque, G.; Bertrand, Y.; Robin, J. Reflectivity of GaTe in the 1 to 35 eV Range. *J. Phys. C: Solid State Phys.* **1977**, *10*, 343−352.
(28) van Smaalen, S. Incommensurate Crystal Structures. *Crystallogr. Rev.* **1995**, *4*, 79−202.
(29) Davis, J. R. *Metals Handbook desk edition*; ASM International: Materials Park, OH, 1998.
(30) Böhm, M.; Huber, G.; MacKinnon, A.; Scharmann, A.; Scharmer, E. G. *Physics of Ternary Compounds/Physik Der Ternären Verbindungen*; Springer-Verlag: Berlin, 1985.
(31) Eichberger, M.; Schäfer, H.; Krumova, M.; Beyer, M.; Demsar, J.; Berger, H.; Moriena, G.; Sciaini, G.; Miller, R. J. D. Snapshots of Cooperative Atomic Motions in the Optical Suppression of Charge Density Waves. *Nature* **2010**, *468*, 799−802.
(32) Zong, A.; Shen, X.; Kogar, A.; Ye, L.; Marks, C.; Chowdhury, D.; Rohwer, T.; Freelon, B.; Weathersby, S.; Li, R.; Yang, J.; Checkelsky, J.; Wang, X.; Gedik, N. Ultrafast Manipulation of Mirror Domain Walls in a Charge Density Wave. *Sci. Adv.* **2018**, *4*, u5501.
(33) Singh, N.; Sharma, P. K. Debye-Waller Factors of Cubic Metals. *Phys. Rev. B* **1971**, *3*, 1141−1148.
(34) Ashcroft, N. W.; Mermin, N. D. *Solid State Physics*; Saunders College: Philadelphia, 1976.
(35) Hill, T. L. *An Introduction to Statistical Thermodynamics*; Dover Publications, Inc.: New York, 1986.
(36) De la Breteque, P. *Gallium Bulletin Bibliographique*; 9, A 15, La Société: Marseille, 1970.
(37) Mamedov, K. K.; Kerimov, I. G.; Mekhtiev, M. P.; Masimov, E. A. Low-Temperature Heat Capacity, Entropy, and Enthalpy of Gallium and Indium Chalcogenides. *Izv. Akad. Nauk SSSR, Neorg. Mater.* **1972**, *8*, 2096.
(38) Harb, M.; Jurgilaitis, A.; Enquist, H.; Nüske, R.; Schmising, C. V. K.; Gaudin, J.; Johnson, S. L.; Milne, C. J.; Beaud, P.; Vorobeva, E.; Caviezel, A.; Mariager, S. O.; Ingold, G.; Larsson, J. Picosecond Dynamics of Laser-Induced Strain in Graphite. *Phys. Rev. B: Condens. Matter Mater. Phys.* **2011**, *84*, 45435.
(39) Ge, S.; Liu, X.; Qiao, X.; Wang, Q.; Xu, Z.; Qiu, J.; Tan, P.; Zhao, J.; Sun, D. Coherent Longitudinal Acoustic Phonon Approaching THz Frequency in Multilayer Molybdenum Disulphide. *Sci. Rep.* **2015**, *4*, 5722.
(40) Harb, M.; Peng, W.; Sciaini, G.; Hebeisen, C. T.; Ernstorfer, R.; Eriksson, M. A.; Lagally, M. G.; Kruglik, S. G.; Miller, R. J. D. Excitation of Longitudinal and Transverse Coherent Acoustic Phonons in Nanometer Free-Standing Films of (001) Si. *Phys. Rev. B: Condens. Matter Mater. Phys.* **2009**, *79*, 94301.
(41) Lobato, I.; Van Dyck, D. MULTEM: A New Multislice Program to Perform Accurate and Fast Electron Diffraction and Imaging Simulations Using Graphics Processing Units with CUDA. *Ultramicroscopy* **2015**, *156*, 9−17.
(42) Ressouche, E.; Loire, M.; Simonet, V.; Ballou, R.; Stunault, A.; Wildes, A. Magnetoelectric $MnPS_3$ as a Candidate for Ferrotoroidicity. *Phys. Rev. B: Condens. Matter Mater. Phys.* **2010**, *82*, 100408R.
(43) Zhang, S.; Mao, N.; Zhang, N.; Wu, J.; Tong, L.; Zhang, J. Anomalous Polarized Raman Scattering and Large Circular Intensity Differential in Layered Triclinic ReS_2. *ACS Nano* **2017**, *11*, 10366−10372.
(44) Jacobsen, R. S.; Andersen, K. N.; Borel, P. I.; Fage-Pedersen, J.; Frandsen, L. H.; Hansen, O.; Kristensen, M.; Lavrinenko, A. V.; Moulin, G.; Ou, H.; Peucheret, C.; Zsigri, B.; Bjarklev, A. Strained Silicon as a New Electro-Optic Material. *Nature* **2006**, *441*, 199−202.
(45) Thompson, J. D.; Zwickl, B. M.; Jayich, A. M.; Marquardt, F.; Girvin, S. M.; Harris, J. G. E. Strong Dispersive Coupling of a High-Finesse Cavity to a Micromechanical Membrane. *Nature* **2008**, *452*, 72−75.
(46) Brown, P. J.; Fox, A. G.; Maslen, E. N.; O'Keefe, M. A.; Willis, B. T. M. Intensity of Diffracted Intensities. In *International Tables for Crystallography*; International Union of Crystallography: Chester, UK, 2006; pp 554−595.

https://dx.doi.org/10.1021/acsnano.0c02643
ACS Nano 2020, 14, 8449−8458